GEOLOGY

Anomalous K-Pg–aged seafloor attributed to impact-induced mid-ocean ridge magmatism

Joseph S. Byrnes[1,2]* and Leif Karlstrom[2]

Eruptive phenomena at all scales, from hydrothermal geysers to flood basalts, can potentially be initiated or modulated by external mechanical perturbations. We present evidence for the triggering of magmatism on a global scale by the Chicxulub meteorite impact at the Cretaceous-Paleogene (K-Pg) boundary, recorded by transiently increased crustal production at mid-ocean ridges. Concentrated positive free-air gravity and coincident seafloor topographic anomalies, associated with seafloor created at fast-spreading rates, suggest volumes of excess magmatism in the range of ~10^5 to 10^6 km^3. Widespread mobilization of existing mantle melt by post-impact seismic radiation can explain the volume and distribution of the anomalous crust. This massive but short-lived pulse of marine magmatism should be considered alongside the Chicxulub impact and Deccan Traps as a contributor to geochemical anomalies and environmental changes at K-Pg time.

INTRODUCTION

The end of the Mesozoic era at ca. 66 million years ago (Ma) is marked by three globally significant events, the Cretaceous-Paleogene (K-Pg) mass extinction, the eruption of the Deccan Traps large igneous province, and the Chicxulub meteorite impact (*1*, *2*). The possibility of connections between these nearly coincident events remains an actively debated topic. Early work speculated that focusing of impact-induced seismic energy triggered large-scale mantle melting and initiated the Deccan flood basalt eruptions. However, detailed eruptive chronology (*3*) and precise dating of both the impact (*4*) and the flood basalts (*5*, *6*) show that the earliest eruptions of the Deccan Traps predate the impact. Simulations further suggest that impact-induced initiation of mantle melting events is unlikely (*7*), especially if the crater basin was rapidly back-filled to compensate ejected mass loss (*8*). Moreover, the impact site is now known to not have been antipodal to Deccan at K-Pg time (*9*). However, recent evidence for a rapid increase in eruption rates (*6*), shifts to lavas of more primitive chemical composition, and changes in feeder dike orientations after the bolide impact (*10*) suggest a possible association between the Chicxulub impact and variations in the progression of Deccan Traps eruptions.

Any triggering of volcanism at the paleo-distances between the Deccan Traps and the Chicxulub crater (*9*) would involve dynamic stresses associated with seismic waves, likely involving orders of magnitude more equivalent energy release than the largest tectonic earthquakes (*11*). Seismic triggering is implicated in some smaller magmatic and hydrologic eruptions (*12*), when existing fluid reservoirs are available for mobilization and are sufficiently sensitive to small stress changes. Earthquakes may also induce non-eruptive volcanic degassing variability (*13*), as might be expected from impulsive changes to subsurface flow pathways. Although large-scale hydrologic response to impacts has been proposed (*14*), volcanism due to impacts is generally hypothesized to be associated with an impact melt sheet or induced mantle decompression melting on a range of time scales (*15*) rather than mobilization of existing stored melt.

If radiated seismic energy did play a role in modulating Deccan eruptions, then other volcanic systems may have been influenced as well. The global mid-ocean ridge (MOR) system is a clear candidate for triggering, with large volumes of partial melt stored in the crust and upper mantle surrounding the ridge axis (*16*, *17*). Oceanic crust records the history of temporal variations in seafloor magmatism continuously and at high resolution through geologic time (*18*). If a transient change in MOR productivity was recorded as anomalous oceanic crust, then the fact that spreading centers are distributed over thousands of kilometers enhances the possibility that even small global perturbations are observable.

We present evidence for a transient change in MOR productivity at K-Pg time. We first demonstrate a change in the global distribution of free-air gravity anomalies above seafloor dated to within 1 million year (My) of the Chicxulub impact, before discussing the characteristics of the seafloor anomalies themselves. Satellite-derived global free-air gravity data (*19*) with a resolution of 1 arc min were high-pass–filtered by subtracting a grid of gravity anomalies that has been averaged over 750 km with the boxcar filter in the GMT software package (*20*). We attribute positive free-air gravity anomalies to locally elevated seafloor topography and by inference crustal thickness anomalies, where an excess volume of melt was extracted from the mantle. We then construct probability density functions (PDFs; defined by a normalized histogram) for the short-wavelength gravity anomalies for seafloor in 1-My age bins up to 100 Ma (*18*, *21*). A bin size of 1 My was chosen because this is the typical uncertainty on the age of the seafloor at a global scale. Errors can be larger than 1 My, where the magnetic anomalies are complex, such as near paleoridge-axis discontinuities [see section S1 and the study of Müller *et al.* (*18*)]. For seafloor older than approximately 20 Ma, the mean errors in the Indian and Pacific oceans are similar to each other.

RESULTS

PDFs for seafloor created at half-spreading rates above 35 mm/year (*18*) are shown in Fig. 1A. Regions of the seafloor within twice the radius of known seamounts (*22*) were removed before binning. The area under a section of a PDF gives the fraction of the seafloor with anomalies in that range. Anomalies are generally not normally distributed, because multiple processes can modify oceanic crust during and after its creation. The mean PDF has a kurtosis of 6, meaning that there are significantly more outlying values than predicted for a Gaussian distribution, and irregular but significant perturbations to the PDFs

[1]Department of Earth Sciences, University of Minnesota, 116 Church Street Southeast, Minneapolis, MN 55455, USA. [2]Department of Earth Sciences, University of Oregon, 1272 University of Oregon, Eugene, OR 97403, USA.
*Corresponding author. Email: jsbyrnes@umn.edu

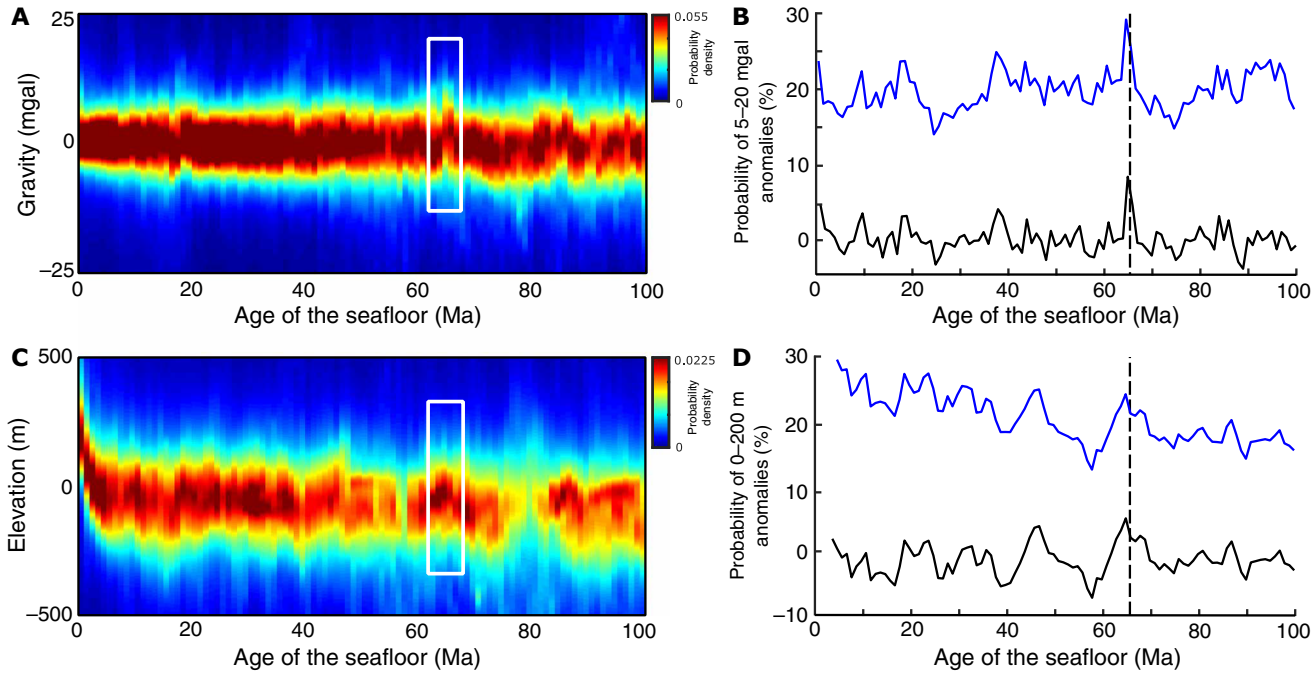

Fig. 1. The distribution of high-passed gravity and topographic anomalies by the age of the seafloor and their relationship to the timing of the Chicxulub impact. (**A**) PDFs for high-passed gravity anomalies by the age of the seafloor. White box highlights K-Pg–aged seafloor. (**B**) The blue line shows probabilities for gravity anomalies between 5 and 20 mgal (in percent). The black line shows the same data after subtracting the median in a 10-My wide moving window. (**C** and **D**) Same as (A) and (B), but for high-passed global seafloor topography.

through time are observed (see section S2). These complex PDFs lead us to analyze the probabilities of anomalies within different gravity ranges.

Gravity anomalies between 5 and 20 mgal are significantly concentrated for seafloor created within 1 My after K-Pg time, with a greater probability of occurrence globally than for any other time up to 100 Ma (blue line in Fig. 1B). To isolate transient features, we subtract the running median with a moving window length of 10 My. For a typical half-spreading rate of 50 mm/year, 10 My equals 500 km of the seafloor in the spreading direction. The transient increase in the probability of 5- to 20-mgal anomalies on K-Pg–aged crust is 8% (black line in Fig. 1B); no other high-pass–filtered global perturbation within the last 100 Ma is greater than 4%. Anomalies in the range of −10 to 0 mgal occur less frequently at K-Pg by approximately the same amount, whereas anomalies outside the range of −10 to 20 mgal do not occur at anomalous rates (see section S2). Nearly antisymmetric transient deviation of negative and positive anomalies with small magnitudes at K-Pg time indicates that perturbations occurred on what would otherwise be normal seafloor, whereas the processes associated with higher-magnitude anomalies, such as fracture zones, were not significantly perturbed at K-Pg time.

K-Pg–aged crust is also associated with an anomalous distribution of seafloor topographic anomalies in the range of 0 to 200 m that coincide with the gravity anomalies (Fig. 1, C and D). The topographic data (*23*) were processed and binned in the same way as the gravity data. PDFs for topography show more long-wavelength and less short-wavelength variability with the age of the seafloor than for gravity. This could arise from greater short-wavelength complexity in the seafloor topography or greater short-wavelength noise associated with estimating bathymetry from gravity (see section S3) (*24*). Global ocean floor topography is derived from either ship board measurements or partially inferred from gravity data, meaning that the topographic data are of variable quality and not entirely independent from the gravity data for wavelengths between 15 and 160 km (*24*). Restricting the topographic data to soundings alone results in approximately an order of magnitude less data (*25*), which are insufficient for our analysis. Therefore, we use the global data set.

Anomalous seafloor is not uniformly distributed among K-Pg–aged crust. We do not observe an anomalous distribution of gravity anomalies for crust created at slow- and intermediate-spreading rates (see section S5). This could be due to the preferential perturbation of faster spreading ridges. Alternatively, the perturbed crust could be hidden among the rough seafloor produced at half-spreading rates below 35 mm/year (*25*). K-Pg–aged seafloor created at faster-spreading rates is concentrated in the modern Pacific and Indian oceans (Fig. 2A), with higher maximum gravity anomalies observed in the Indian Ocean versus the Pacific Ocean (Fig. 2B). Neither the distribution of the perturbed seafloor nor the magnitude of the gravity anomalies appears to be related to the location of the Chicxulub impact or its antipode at K-Pg time (Fig. 2B).

In these faster segments, anomalies cluster in irregularly shaped features that do not immediately stand out from the background roughness of the seafloor at available resolution (*25*). However, when compared to similar features before and after the impact (see section S3), anomalies overlapping with K-Pg–aged crust are more areally extensive, are more variable in area, and have larger volumes (Fig. 3A, left scale). Despite the larger maximum gravity anomalies in the Indian Ocean, a peak in the concentration of anomalies between 5 and 20 mgal with a value of 8% at K-Pg is independently observed in both the modern Pacific and Indian oceans (Fig. 4A), which confirms the global

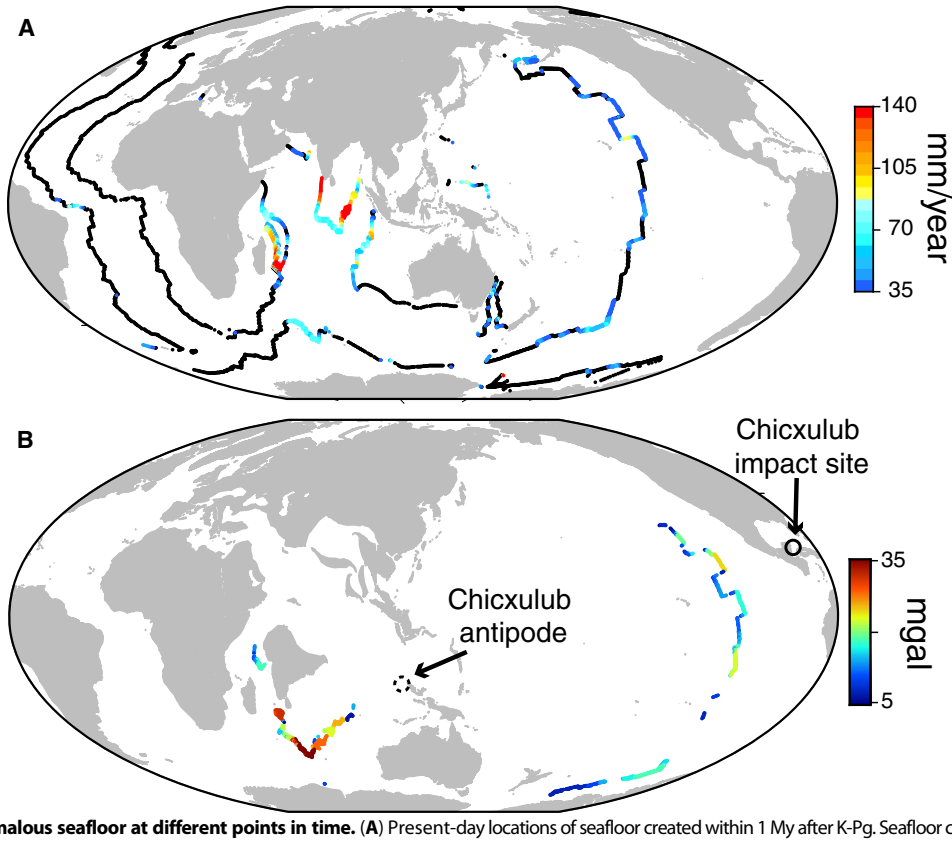

Fig. 2. Locations of anomalous seafloor at different points in time. (**A**) Present-day locations of seafloor created within 1 My after K-Pg. Seafloor created at half-spreading rates above and below 35 mm/year are in colors and black, respectively. (**B**) Reconstruction with GPlates (*49*) of fast-spreading seafloor to locations at K-Pg time. Colors show the maximum gravity anomaly within 2° of the location before reconstruction.

extent of this feature. The high amplitude feature is sharply demarcated to a duration of 1 My in the global average and in the Indian Ocean and extends over 3 My in the Pacific Ocean. Given the uncertainties in seafloor age and potential for distributed lava flows or off-axis volcanism (*26*) on older crust to broaden even brief events, we do not attempt to localize these features further in time.

Features other than the peak near K-Pg are less certain. No transient concentration of the gravity anomalies exceeds half the amplitude (8%) of the K-Pg–aged peak (black line in Fig. 1B). The second largest peak in Fig. 1B occurs at 37 to 38 Ma, within 1 to 2 My of the largest known bolide impacts to occur within the last 100 My other than Chicxulub: the Popigai and Chesapeake Bay events (*27*). The large-amplitude gravity anomaly in the Indian Ocean at this time may be influenced by the Kerguelen Plateau (*28*); however, there is a small peak in the Pacific Ocean, so a global feature cannot be ruled out. Other peaks in the data are not coherent between the two oceanic basins, and there is insufficient fast-spreading crust elsewhere for independent analysis. Finally, there is no evidence for periodic signals in the curves of Fig. 1B because their power spectra are essentially white.

DISCUSSION

The potential significance of transiently increased MOR productivity at K-Pg time depends largely on the total volume of the excess magmatic products. A lower bound comes from summing up the volumes of anomalous crust with gravity anomalies above the noise floor (we impose a threshold of >5 mgal) with elevation above the mean local sea depth. The result is 2×10^4 to 3×10^4 km^3 larger anomaly volumes than

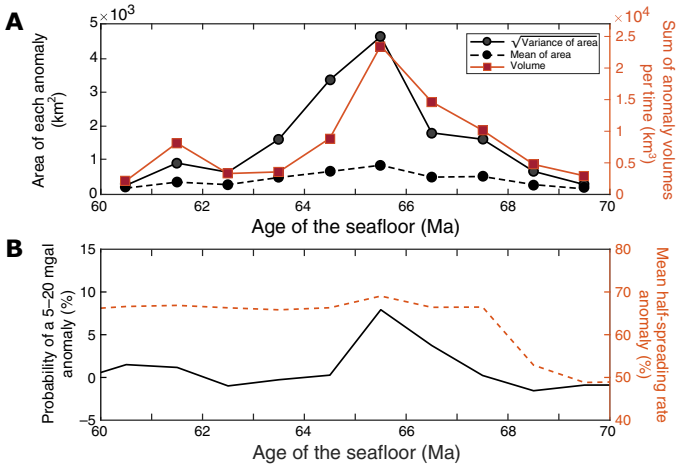

Fig. 3. Morphology and context for the seafloor anomalies. (**A**) Distributions of anomalies near K-Pg–aged crust derived from global seafloor gravity and topography data from 60 to 70 Ma. Dashed and solid black lines (left axis) show the lognormal mean area and variance of contiguous regions exhibiting gravity anomalies greater than 5 mgal against the mean age in 1-My bins. Red line (right axis) shows the corresponding total volume of these anomalies above the mean elevation of surrounding seafloor. (**B**) Comparison of detrended gravity anomalies from Fig. 1B with the mean half-spreading rate for crust created at half-spreading rates above 35 mm/year.

before or after K-Pg (Fig. 3A, red curve, right scale). Such an estimate does not account for intrusions or lithospheric flexure and neglects the potential for anomalies among the complex bathymetry created at intermediate- and slow-spreading rates.

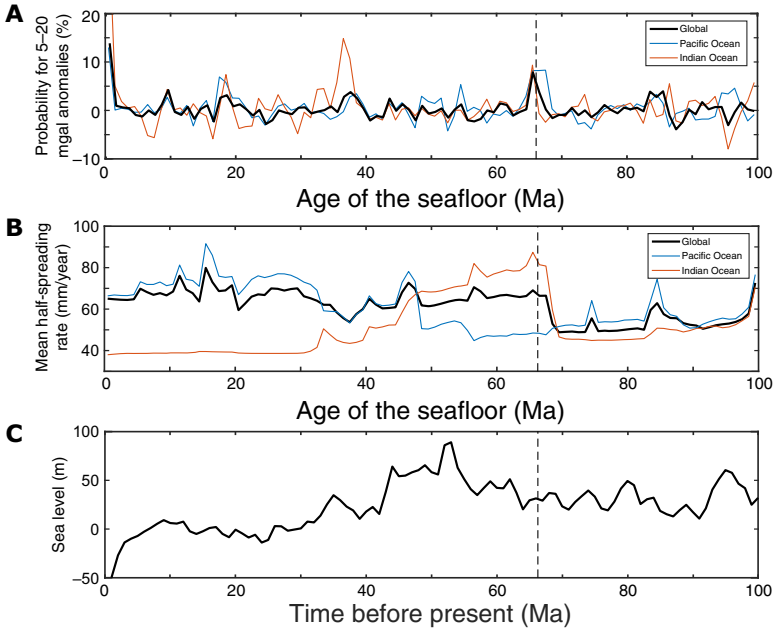

Fig. 4. Comparison between oceanic gravity anomalies and other metrics of geologic change over the last 100 Ma. The vertical dashed line in all panels marks K-Pg. (**A**) The probabilities of gravity anomalies between 5 and 20 mgal for all fast-spreading seafloor and for fast-spreading seafloor in the Pacific and Indian oceans are shown by the black, blue, and orange lines, respectively. The median in a 10-My wide moving window has been subtracted from each curve. (**B**) Average half-spreading rates for seafloor created at half-spreading rates above 35 mm/year for the globe, Pacific Ocean, and Indian Ocean are shown by the black, blue, and orange lines, respectively. (**C**) Global sea level over the past 100 My (*39*) resampled to 1-My intervals. Values are relative to the present day.

A more refined total volume estimate comes from modeling the magnitude and duration of the global gravity and topographic anomalies averaged over all K-Pg–aged seafloor (Fig. 1). We assume that excess magmatism is partitioned between the surface and the lower crust (section S4), creating topography whose magnitude depends on the flexural wavelength of the crust compared to the dimensions of applied loads, as well as the relative densities of the oceanic crust and mantle. The observed gravity and topography do not uniquely constrain the elastic thickness or the partitioning of magma between the surface and the subsurface (*29*). Although the transfer function between gravity and topography depends upon the thickness of the elastic lithosphere, the anomalies are generally small enough that they may be only partially compensated, even with the low elastic thicknesses at MORs (section S4). We can match the range of the observed gravity and topographic anomalies with volumes (per ridge length) in the range of ~3 to 65 km^3/km. Larger values are generally associated with higher intruded fractions. Scaling this over the ~60,000 km of MOR (*30*) present at 66 Ma gives a total volume excess crust of ~2×10^5 to 6×10^6 km^3. This volume estimate assumes that eruptions are distributed across the whole MOR system and not only the ridge segments where we constrain the anomalies in the Indian and Pacific oceans (Fig. 2). There are insufficient data to directly constrain a scaling of enhanced magmatism over the entire MOR system (Figs. 1 and 2), so the larger volume estimates are an upper bound. The direct summation of excess volumes (Fig. 3A) is a lower bound.

These observations are consistent with enhanced melt delivery to the ridge due to rapid changes in mantle melt transport capacity after the Chicxulub impact. Increasing the volume of melt transported to the ridge could leave behind free-air gravity anomalies by thickening the crust at the ridge axis and by increasing the pressure head driving lava extrusion (*31*). The predicted time scales for post-impact permeability increases and structural relaxation back to pre-impact values are likely shorter duration (10^3 to 10^5 years) (*10*, *32*) than the 1- to 3-My seafloor age band for which the anomaly is observed (Fig. 4A) and the estimated period of accelerated Deccan eruptions (*6*). Therefore, this mechanism requires either that seafloor ages are not sufficiently precise or that anomalous magmatism obscures normal ocean floor stratigraphy. For example, submarine lava flows are thicker and longer than their subareal counterparts because of lower effective gravity and better insulation (*33*). Sheet-like flow sequences (tens of kilometers long) in the range of ~200 m thick are sufficient to reproduce the observed gravity anomalies. Other possible origins of apparently acausal anomalies include ridge-axis discontinuities and off-axis volcanism, the latter of which can be productive up to several hundred kilometers from the ridge axis in the modern Pacific Ocean (*26*).

Melt fractions on the order of a few percent or less in the mantle are required to explain our estimated volumes of excess crust (see section S4). The volume of melt retained in the mantle beneath modern MORs can be estimated from electrical and seismic models, although conversions to melt fractions are uncertain. Estimates of melt fractions of 1 to 3% in a triangular region beneath the northern East Pacific Rise (*16*) imply melt volumes of 40 to 120 km^3/km. Estimates of 0.5% melt within a region extending 50 to 100 km from the Juan de Fuca Ridge (*17*) imply melt volumes of 20 to 40 km^3/km. On the basis of these estimates, our lower bound on the amount of excess erupted material (3 km^3/km) is possible if approximately $^1/_{10}$ of the in situ melt is released, whereas the upper bound (65 km^3/km) is possible if most or all of the available melt is released. Thus, there is no need to appeal to enhanced MOR mantle melting after the impact but only to the increased mobility of existing partial melt.

Triggering of magmatism by the Chicxulub impact is better able to explain these observations than alternative hypotheses. We disfavor mantle plume activity alone as an explanation for the observations, because concentrated gravity anomalies exist in both the Indian and Pa-

cific oceans (Fig. 4A). We consider changes in plate motions near K-Pg time (*34*–*36*) as a plausible and alternative explanation for our observations. In particular, it is possible that large gravity anomalies in the Indian Ocean are influenced by increased spreading rates attributed to the mantle plume responsible for the Deccan Traps (*35*). However, the duration of the gravity signature is impulsive compared to a long-lived increase in spreading rates, and the change in spreading rates begins 2 to 3 My before the impact when the peak anomaly is observed (Figs. 3B and 4B). Moreover, the anomalous gravity signature is global, whereas the change in spreading rates in the Pacific Ocean at K-Pg time (Fig. 4B) is small and of the opposite sign as the change in the Indian Ocean. We also note that other large changes in spreading rate do not correlate with gravity anomalies. Finally, a global reduction in sea level near K-Pg may have occurred (*37*), which could induce pressure-release melting, as has been proposed to explain topographic variability on the seafloor (*38*). However, estimated changes in sea level (Fig. 4C) at K-Pg are not anomalous in a Cenozoic context (*39*). Sea level, in general, does not correlate well with the global gravity time series. The correlation coefficient with the distribution of gravity anomalies (blue line in Fig. 1B) and sea levels up to 100 Ma is only 0.13.

If eruptions at oceanic ridges were enhanced by the Chicxulub impact, then it is more plausible that the Deccan Traps were enhanced as well. The largest-scale seismic triggering of magmatism known would then be a global magmatic episode at the end of the Cretaceous period. The marine magmatic episode may be more akin to oceanic plateau volcanism than normal MOR activity because of the large volume and short duration. The results presented here, along with previous works on the Deccan Traps (*6*, *10*), motivate a sequence of events at K-Pg time, where the Chicxulub impact is followed by triggered eruptions of the Deccan Traps and the global MOR system. A diverse array of volcanic and hydrologic systems responds to seismic stresses (*12*, *13*), so impulsive impact-induced activity at K-Pg time may not have been limited to MORs and the Deccan Traps.

Currently available data are insufficient to tightly constrain the scale of the marine eruptions or their impact on marine environments, but our modeling suggests significant volumes comparable to the total volume of the Deccan Traps (*10*). Better volume estimates, particularly constraints at slower-spreading rates, may be possible with more high-resolution topographic data. But even for fast-spreading environments, our analysis could underestimate the scale of MOR activity at K-Pg time. Free-air gravity anomalies are unlikely to reveal variations in crustal thickness created in the wake of second-order discontinuities at the paleoridge axis (*40*), and magmatic intrusions have a weaker free-air gravity signature than surface loads. Both large-scale submarine lava flows (*41*) and intrusions (*42*, *43*) could increase hydrothermal activity, so the cumulative environmental impact of these magmatic events may have been significant.

We hypothesize that a pulse of global marine volcanism played an important role in the environmental crises at the end of the Cretaceous. MOR volcanism can perturb the oceanic environment directly through magmatism by extruding large volumes of basalt and releasing volcanic gases (*41*) or through enhanced hydrothermal venting driven by magmatic intrusion. A negative $\delta^{13}C$ shift of similar magnitude in both terrestrial and marine environments is observed at K-Pg time, but isotopic values recovered to pre–K-Pg values on a time scale shorter by several orders of magnitude on land than in the sea (*4*). Both the magnitude and duration of the $\delta^{13}C$ signal are difficult to attribute to biological processes alone (*44*). Light $\delta^{13}C$ values, due to the production of methane, have been recorded in hydrothermal plumes at active MOR vents (*45*), and so marine volcanism may have played an enhanced role in the K-Pg carbon cycle. Similarly, fresh basalts and hydrothermal fluids are a primary source of light $\delta^{7}Li$ isotopes in seawater, which underwent a rapid and negative shift (~5‰ over ~500 thousand years) at K-Pg time (*46*). Marine volcanism also provides a potential source of oceanic acidification, which is suggested by the fossil record but cannot be explained by currently known sources of acidification (*47*).

MATERIALS AND METHODS

The materials used in this study were publicly available data sets for the age of the oceanic crust, marine gravity anomalies, and global topography. These data sets were available as described in the Acknowledgments section, and any subsequent processing of these data sets was described in the main text and in the Supplementary Materials. To make estimates of the excess volumes erupted at K-Pg time, we used global topographic and gravity anomalies at K-Pg time to constrain one-dimensional models for enhanced crustal production at MORs, accounting for the flexural response of anomalous loading from a combination of intrusions and excess surface lava extrusion. We implement the Fourier domain technique of Forsyth *et al.* (*26*) and Ali *et al.* (*48*), as described in section S4. This procedure constrains the ratio of intruded to extruded loads, assumed to be spatially in phase, that explain the range of the observed gravity and topography anomalies. We show that these anomalies are most sensitive to the ratio of loads at the base versus at the top of the crust (that is, the ratio of magmatic intrusion to extrusion) with a Monte Carlo search that also samples crustal density, the thickness of the elastic lithosphere, and anomaly geometry parameters (see section S4).

SUPPLEMENTARY MATERIALS

Supplementary material for this article is available at http://advances.sciencemag.org/cgi/content/full/4/2/eaao2994/DC1

section S1. Uncertainties of and modifications to the ages of the seafloor

section S2. Probability distribution functions for all and K-Pg–aged crust

section S3. Examples of anomalous seafloor created at K-Pg time with volume and area estimates

section S4. Modeling of gravity anomalies

section S5. Probability distribution functions for crust created at slow- and intermediate-spreading rates

fig. S1. Mean error of the seafloor from the study of Müller *et al.* (*18*).

fig. S2. Comparison between the PDFs for gravity anomalies for all and K-Pg–aged crust.

fig. S3.Example gravity and topographic anomalies on K-Pg–aged crust.

fig. S4. Profiles of flexurally adjusted surface (top) and Moho (middle) topography, along with free-air gravity anomaly (bottom), for a rectangular load at both top and bottom of an initially 6-km-thick plate.

fig. S5. Required and available volumes of basalt.

fig. S6. Compare Fig. 1 (A and B) of the main text.

References (*50*–*54*)

REFERENCES AND NOTES

1. L. W. Alvarez, W. Alvarez, F. Asaro, H. V. Michel, Extraterrestrial cause for the Cretaceous-Tertiary extinction. *Science* **208**, 1095–1108 (1980).
2. P. Schulte, L. Alegret, I. Arenillas, J. A. Arz, P. J. Barton, P. R. Bown, T. J. Bralower, G. L. Christeson, P. Claeys, C. S. Cockell, G. S. Collins, A. Deutsch, T. J. Goldin, K. Goto, J. M. Grajales-Nishimura, R. A. Grieve, S. P. Gulick, K. R. Johnson, W. Kiessling, C. Koeberl, D. A. Kring, K. G. MacLeod, T. Matsui, J. Melosh, A. Montanari, J. V. Morgan, C. R. Neal, D. J. Nichols, R. D. Norris, E. Pierazzo, G. Ravizza, M. Rebolledo-Vieyra, W. U. Reimold, E. Robin, T. Salge, R. P. Speijer, A. R. Sweet, J. Urrutia-Fucugauchi, V. Vajda, M. T. Whalen, P. S. Willumsen, The Chicxulub asteroid impact and mass extinction at the Cretaceous-Paleogene boundary. *Science* **327**, 1214–1218 (2010).
3. N. Bhandari, P. N. Shukla, Z. G. Ghevariya, S. M. Sundaram, Impact did not trigger Deccan volcanism: Evidence from Anjar K/T boundary intertrappean sediments. *Geophys. Res. Lett.* **22**, 433–436 (1995).

4. P. R. Renne, A. L. Deino, F. J. Hilgen, K. F. Kuiper, D. F. Mark, W. S. Mitchell III, L. E. Morgan, R. Mundil, J. Smit, Time scales of critical events around the Cretaceous-Paleogene boundary. *Science* **339**, 684–687 (2013).
5. B. Schoene, K. M. Samperton, M. P. Eddy, G. Keller, T. Adatte, S. A. Bowring, S. F. R. Khadri, B. Gertsch, U-Pb geochronology of the Deccan Traps and relation to the end-Cretaceous mass extinction. *Science* **347**, 182–184 (2015).
6. P. R. Renne, C. J. Sprain, M. A. Richards, S. Self, L. Vanderkluysen, K. Pande, State shift in Deccan volcanism at the Cretaceous-Paleogene boundary, possibly induced by impact. *Science* **350**, 76–78 (2015).
7. B. A. Ivanov, H. J. Melosh, Impacts do not initiate volcanic eruptions: Eruptions near the crater. *Geology* **31**, 869–872 (2003).
8. J. Ebbing, P. Janle, J. Koulouris, B. Milkereit, 3D gravity modelling of the Chicxulub impact structure. *Planet. Space Sci.* **49**, 599–609 (2001).
9. S. Chatterjee, A. Goswami, C. R. Scotese, The longest voyage: Tectonic, magmatic, and paleoclimatic evolution of the Indian plate during its northward flight from Gondwana to Asia. *Gondw. Res.* **23**, 238–267 (2013).
10. M. A. Richards, W. Alvarez, S. Self, L. Karlstrom, P. R. Renne, M. Manga, C. J. Sprain, J. Smit, L. Vanderkluysen, S. A. Gibson, Triggering of the largest Deccan eruptions by the Chicxulub impact. *GSA Bull.* **127**, 1507–1520 (2015).
11. M. A. Meschede, C. L. Myhrvold, J. Tromp, Antipodal focusing of seismic waves due to large meteorite impacts on Earth. *Geophys. J. Int.* **187**, 529–537 (2011).
12. M. Manga, E. Brodsky, Seismic triggering of eruptions in the far field: Volcanoes and geysers. *Annu. Rev. Earth Planet. Sci.* **34**, 263–291 (2006).
13. D. M. Avouris, S. A. Carn, G. P. Waite, Triggering of volcanic degassing by large earthquakes. *Geology* **45**, 715–718 (2009).
14. C.-y. Wang, M. Manga, A. Wong, Floods on Mars released from groundwater by impact. *Icarus* **175**, 551–555 (2005).
15. A. P. Jones, Impact volcanism and mass extinctions, in *Volcanism, Impacts, and Mass Extinctions: Causes and Effects*, G. Keller, A. C. Kerr, Eds. (Geological Society of America, 2014), vol. Special Paper 505, pp. 369–381.
16. K. Key, S. Constable, L. Liu, A. Pommier, Electrical image of passive mantle upwelling beneath the northern East Pacific Rise. *Nature* **495**, 499–502 (2013).
17. J. S. Byrnes, D. R. Toomey, E. E. E. Hooft, J. Nábělek, J. Braunmiller, Mantle dynamics beneath the discrete and diffuse plate boundaries of the Juan de Fuca plate: Results from Cascadia Initiative body wave tomography. *Geochem. Geophys. Geosyst.* **18**, 2906–2929 (2017).
18. R. D. Müller, M. Sdrolias, C. Gaina, W. R. Roest, Age, spreading rates and spreading symmetry of the world's ocean crust. *Geochem. Geophys. Geosyst.* **9**, Q04006 (2008).
19. D. T. Sandwell, R. D. Müller, W. H. F. Smith, E. Garcia, R. Francis, New global marine gravity model from CryoSat-2 and Jason-1 reveals buried tectonic structure. *Science* **346**, 65–67 (2014).
20. P. Wessel, W. H. F. Smith, R. Scharroo, J. Luis, F. Wobbe, Generic mapping tools: Improved version released. *Eos Trans. AGU* **94**, 409–410 (2013).
21. S. C. Cande, D. V. Kent, Revised calibration of the geomagnetic polarity timescale for the Late Cretaceous and Cenozoic. *J. Geophys. Res.* **100**, 6093–6095 (1995).
22. P. Wessel, D. T. Sandwell, S. S. Kim, The global seamount census. *Oceanography* **23**, 24–33 (2010).
23. C. Amante, B. W. Eakins, *ETOPO1 1 Arc-Minute Global Relief Model: Procedures, Data Sources and Analysis* (NOAA Technical Memorandum NESDIS NGDC-24, National Geophysical Data Center, NOAA, 2009).
24. W. H. F. Smith, D. T. Sandwell, Bathymetric prediction from dense satellite altimetry and sparse shipboard bathymetry. *J. Geophys. Res.* **99**, 21803–21824 (1994).
25. W. H. F. Smith, Seafloor tectonic fabric from satellite altimetry. *Annu. Rev. Earth Planet. Sci.* **26**, 697–738 (1998).
26. D. W. Forsyth, N. Harmon, D. S. Scheirer, R. A. Duncan, Distribution of recent volcanism and the morphology of seamounts and ridges in the GLIMPSE study area: Implications for the lithospheric cracking hypothesis for the origin of intraplate, non-hot spot volcanic chains. *J. Geophys. Res.* **111**, B11407 (2006).
27. B. Schmitz, S. Boschi, A. Cronholm, P. R. Heck, S. Monechi, A. Montanari, F. Terfelt, Fragments of Late Eocene Earth-impacting asteroids linked to disturbance of asteroid belt. *Earth Planet. Sci. Lett.* **425**, 77–83 (2015).
28. R. D. Müller, C. Gaina, S. Clark, Seafloor spreading around Australia, in *Billion-Year Earth History of Australia and Neighbors in Gondwanaland*, J. J. Veeverd, Ed. (GEMOC Press, 2000), pp 18–28.
29. D. W. Forsyth, Subsurface loading and estimates of the flexural rigidity of continental lithosphere. *J. Geophys. Res.* **90**, 12623–12632 (1985).
30. M. Seton, C. Gaina, R. D. Müller, C. Heine, Mid-Cretaceous seafloor spreading pulse: Fact or fiction? *Geology* **37**, 687–690 (2009).
31. J.-A. Olive, M. D. Behn, G. Ito, W. R. Buck, J. Escartín, S. Howell, Sensitivity of seafloor bathymetry to climate-driven fluctuations. *Science* **350**, 310–313 (2015).
32. M. Manga, J. C. Rowland, Response of Alum Rock springs to the October 30, 2007 Alum Rock earthquake and implications for the origin of increased discharge after earthquakes. *Geofluids* **9**, 237–250 (2009).
33. T. K. P. Gregg, D. J. Fornari, Long submarine lava flows: Observations and results from numerical modeling. *J. Geophys. Res.* **103**, 27517–27531 (1998).
34. S. C. Cande, D. R. Stegman, Indian and African plate motions driven by the push force of the Réunion plume head. *Nature* **475**, 47–52 (2011).
35. P. Glišović, A. M. Forte, On the deep-mantle origin of the Deccan Traps. *Science* **355**, 613–616 (2017).
36. M. Li, B. Black, S. Zhong, M. Manga, M. L. Rudolph, P. Olson, Quantifying melt production and degassing rate at mid-ocean ridges from global mantle convection models with plate motion history. *Geochem. Geophys. Geosyst.* **17**, 2884–2904 (2016).
37. B. U. Haq, Cretaceous eustasy revisited. *Global Planet. Change* **113**, 44–58 (2014).
38. J. W. Crowley, R. F. Katz, P. Huybers, C. H. Langmuir, S.-H. Park, Glacial cycles drive variations in the production of oceanic crust. *Science* **347**, 1237–1240 (2015).
39. K. G. Miller, M. A. Kominz, J. V. Browning, J. D. Wright, G. S. Mountain, M. E. Katz, P. J. Sugarman, B. S. Cramer, N. Christie-Blick, S. F. Pekar, The Phanerozoic record of global sea-level change. *Science* **310**, 1293–1298 (2005).
40. D. R. Toomey, E. E. E. Hooft, Mantle upwelling, magmatic differentiation, and the meaning of axial depth at fast-spreading ridges. *Geology* **36**, 679–682 (2008).
41. T. M. Gernon, T. K. Hincks, T. Tyrrell, E. J. Rohling, M. R. Palmer, Snowball Earth ocean chemistry driven by extensive ridge volcanism during Rodinia breakup. *Nat. Geosci.* **9**, 242–248 (2016).
42. W. S. Wilcock, E. E. E. Hooft, D. R. Toomey, P. R. McGill, A. H. Barclay, D. S. Stakes, T. M. Ramirez, The role of magma injection in localizing black-smoker activity. *Nat. Geosci.* **2**, 509–513 (2009).
43. G. M. Arnoux, D. R. Toomey, E. E. E. Hooft, W. S. D. Wilcock, J. Morgan, M. Warner, B. P. VanderBeek, Seismic evidence that black smoker heat flux is influenced by localized magma replenishment and associated increases in crustal permeability. *Geophys. Res. Lett.* **44**, 1687–1695 (2017).
44. E. Thomas, Cenozoic mass extinctions in the deep sea: What perturbs the largest habitat on Earth? *Geol. Soc. Am. Spec. Pap.* **424**, 1–23 (2007).
45. M. Lilley, D. A. Butterfield, E. J. Olson, J. E. Lupton, S. A. Macko, R. E. McDuff, Anomalous CH_4 and NH_4^+ concentrations at an unsedimented mid-ocean-ridge hydrothermal system. *Nature* **364**, 45–47 (1993).
46. S. Misra, P. N. Froelich, Lithium isotope history of Cenozoic seawater: Changes in silicate weathering and reverse weathering. *Science* **335**, 818–823 (2012).
47. T. Tyrrell, A. Merico, D. I. A. McKay, Severity of ocean acidification following the end-Cretaceous asteroid impact. *Proc. Natl. Acad. Sci. U.S.A.* **112**, 6556–6561 (2015).
48. M. Y. Ali, A. B. Watts, I. Hill, A seismic reflection profile study of lithospheric flexure in the vicinity of the Cape Verde Islands. *J. Geophys. Res.* **108**, 2239 (2003).
49. M. Gurnis, M. Turner, S. Zahirovic, L. DiCaprio, S. Spasojevic, R. D. Müller, J. Boyden, M. Seton, V. C. Manea, D. J. Bower, Plate tectonic reconstructions with continuously closing plates. *Comput. Geosci.* **38**, 35–42 (2012).
50. J. A. Goff, W. H. F. Smith, K. M. Marks, The contributions of abyssal hill morphology and noise to altimetric gravity fabric. *Oceanography* **17**, 24–37 (2004).
51. G. Ito, A. Taira, Compensation of the Ontong Java Plateau by surface and subsurface loading. *J. Geophys. Res.* **105**, 11171–11183 (2000).
52. A. B. Watts, *Isostasy and Flexure of the Lithosphere* (Cambridge Univ. Press, 2001).
53. H. J. A. van Avendonk, J. K. Davis, J. L. Harding, L. A. Lawver, Decrease in oceanic crustal thickness since the breakup of Pangea. *Nat. Geosci.* **10**, 58–61 (2016).
54. S. M. White, J. A. Crisp, F. J. Spera, Long-term volumetric eruption rates and magma budgets. *Geochem. Geophys. Geosyst.* **7**, Q03010 (2006).

Acknowledgments: We thank M. A. Richards for reading an early version of this manuscript and M. Manga, D. R. Toomey, and W. Alvarez for discussions. Comments by two referees and associate editor B. Schoene significantly improved the presentation of this manuscript. **Funding:** L.K. acknowledges support from NSF EAR 1624557. **Author contributions:** J.S.B. and L.K. both conceived the study and wrote the paper. J.S.B. processed and analyzed the data. L.K. developed models and performed image processing. **Competing interests:** All authors declare that they have no competing interests. **Data and materials availability:** All data used in this paper are available from the following sources. Free-air gravity anomalies were made available by the Scripps Institution of Oceanography at the University of California San Diego (ftp://topex.ucsd.edu/pub/global_grav_1min/, item grav.24.1.img). Ages and spreading rates were made available by the EarthByte group at the University of Sydney (ftp://ftp.earthbyte.org/earthbyte/agegrid/2008/Grids/, items age.3.6.xyz, rate.3.6.xyz, and error.3.6.xyz). The topographic data were made available by the National Geophysical Data Center of the National Oceanic and Atmospheric Administration (https://ngdc.noaa.gov/mgg/global/relief/ETOPO1/data/, item ETOPO1_Bed_g_ gmt4.grd.gz). Processed versions of these data, as described in the text, are available from the authors upon request.

Submitted 5 July 2017
Accepted 9 January 2018
Published 7 February 2018
10.1126/sciadv.aao2994

Citation: J. S. Byrnes, L. Karlstrom, Anomalous K-Pg–aged seafloor attributed to impact-induced mid-ocean ridge magmatism. *Sci. Adv.* **4**, eaao2994 (2018).